Eur. Phys. J. Plus (2021) 136:22
https://doi.org/10.1140/epjp/s13360-020-00974-9

THE EUROPEAN PHYSICAL JOURNAL PLUS

Regular Article

A detailed study of nuclear structure of odd-mass Pm isotopes near $N = 82$ shell closure

Veerta Rani[1], Amit Kumar[2], Suram Singh[1,a], Manvi Rajput[1], Arun Bharti[3], G. H. Bhat[2], J. A. Sheikh[4]

[1] Department of Physics and Astronomical Sciences, Central University of Jammu, Samba, J&K 181143, India
[2] Higher Education Department, Government of Jammu and Kashmir, Srinagar, J&K, India
[3] Department of Physics, University of Jammu, Jammu 180001, India
[4] Department of Physics, University of Kashmir, Srinagar, J&K 190001, India

Received: 3 August 2020 / Accepted: 28 November 2020

Abstract A systematic study of the positive as well as negative parity yrast structure for the odd-mass $^{145-149}$Pm isotopes is carried out by using the angular momentum projection technique implemented in the projected shell model (PSM). By assuming an axial symmetry in the deformed basis, we have been able to calculate the yrast states up to a maximum spin of 47/2 for both positive and negative parity, and as a result, a good agreement is obtained with available experimental data for all isotopes. The intrinsic structure of positive and negative parity yrast states has been found to be built on $\pi g_{7/2} \otimes \nu h_{11/2}$ and $\pi h_{11/2} \otimes \nu h_{11/2}$ configurations, respectively. The phenomenon of back-bending has also been discussed in the present work. Reduced electric and magnetic transitions probabilities [$B(E2)$ and $B(M1)$] are also calculated using the PSM wave functions. Since experimental data on $B(E2)$ and $B(M1)$ are not available, these results can serve as motivation for experimentalists to look for these data. However, the theoretical values of transition strength ratio $B(M1)/B(E2)$ have been found to be matching excellently with the experimental ones.

1 Introduction

The rare-earth nuclei with $N = 88$–90 are well known to have shape transition from nearly spherical or weakly deformed shapes for $N < 88$ to well-deformed shapes for $N > 90$. The nuclei with $N = 88$–90 lie in a transition region where shape changes from spherical to quadrupole prolate deformation. The successful application of shell model on the nuclei lying near $N = 82$ shell closure, to interpret the high-spin states of several nuclei in this region, shows that nuclei in this mass region are sufficiently spherical to allow a single-particle model description of their properties [1–4]. Further, the many-body nuclear correlations in this region can play an important role and lead to various shapes other than those that are spherically symmetric like reflection symmetric prolate or oblate shapes having quadrupole deformation, triaxial shapes, etc. Thus, this region has proved to be a fruitful testing ground for the study of single-particle excitations at high angular momenta. Long time ago, it has been recognized that octupole

[a] e-mail: suramsingh@gmail.com (corresponding author)

Published online: 03 January 2021

collectivity is an important component of nuclear excitations in nuclei around $N = 82$ region [5]. In heavier lanthanides, this collectivity gives rise to a possible octupole deformation [6–9]. In lighter isotopes, it manifests itself by octupole vibrations coupled to multi-particle configurations. A variety of such excitations have been found in the $N = 85$, even-Z isotones and in ^{148}Eu [8]. A similar situation is expected in the Pm isotopes as previous study of high-spin states [10] in promethium (Pm) isotopes with $Z = 61$ nuclei provided evidence that the yrast spectrum of Pm isotopes can be interpreted in terms of the weak coupling of unpaired $d_{5/2}$, $g_{7/2}$ and $h_{11/2}$ proton holes and protons to a Nd core. Moreover, promethium isotopes lie in the region of transitional lanthanides where evidence has been found suggesting the presence of octupole deformation [8]. Therefore, one may expect that its excitation pattern will be dominated by single-particle configurations and vibration like collective excitations. Pronounced octupole excitations, observed in the neighbouring nuclei (like ^{149}Tb [11]), suggest that octupole collectivity may play an important role in the excitation mechanism of odd-mass Pm nuclei having neutron number between 82 and 90. Further, the heavier isotopes of rare-earth region, which are mostly neutron rich, can be accessed by the fission process. The spectroscopy of heavy fission fragments provides the opportunity to investigate deformation effects as a function of neutron number for a particular isotopic chain. Pm nuclei, with a wide isotopic range, are good candidates to explore the evolution of deformation with neutron number and possible role of deformation in this region. It may be noted that there are no stable isotopes of Pm, and moreover, the isotopes beyond ^{151}Pm are known only through radioactive decay studies [12–20]. Extensive studies of odd-A nuclei, in the past, have resulted in a good understanding of the coupling between an unpaired valence nucleon and an even–even core nucleus in cases where the core nucleus is either well deformed or spherical. But particle–core coupling behaviour is not so well understood in nuclei which lie in between these two limiting shapes. However, various studies were made in the past to understand this behaviour. Ch. Vieu et al. [21] studied high-spin states in ^{145}Pm with TESSA3 operating at NSF Daresbury, through the ^{134}Xe (^{15}N, 4n) compound nucleus reaction using a solid xenon target and proposed an extended level scheme of ^{145}Pm. W. Urban et al. [22] studied excited states in ^{147}Pm through the ^{136}Xe (^{15}N, 4n) and ^{148}Nd (d, 3n) compound nucleus reactions. A solid xenon target has been used to populate high-spin states in ^{147}Pm. The half-life of the isomeric level at 649.3 keV has been remeasured to be 27 ± 3 ns. An extended level scheme is proposed, which is discussed in terms of single-particle excitations and collective quadrupole and octupole vibrations coupled to them. The possible presence of octupole deformation is considered. M.A. Jonnes et al. [23] have studied the transitional lanthanide nucleus ^{149}Pm through the reaction ^{150}Nd (d, 3n). The level scheme of this nucleus was extended up to $27/2^-$, and the excited levels have been found to build over $\pi h_{11/2}$ state.

In our previous work [24], we have already described the structure of $^{131-139}$Pm isotopes and all these isotopes lie below the $N = 82$ shell closure. Moreover, in our recent work on $^{151-161}$Pm isotopes [25], we have successfully not only confirmed the recently reported experimental/theoretical data but also extended the already available information on the energy levels and added new information on the reduced transition probabilities. It should be noted that all Pm isotopes with $A > 151$ lie above the $N = 92$ subshell closure. Thus, the main motive to carry out the present piece of work is to study the deformation trend in Pm isotopes lying between $N = 82$ shell closure and $N = 92$ subshell closure. Moreover, the presence of $Z = 64$ subshell closure [26] makes ^{145,147,149}Pm isotopes ($Z = 61$) interesting candidates for investigating onset of deformation near subshell/shell closure. With this motivation, we have carried out PSM calculations on odd-mass $^{145-149}$Pm and have analysed the calculated results in the context of physics. Various properties obtained through PSM calculations are compared with the available experimental data. The paper is arranged as follows. An outline

of the PSM is given in Sect. 2. Theoretical discussion and comparison with experimental data are presented in Sect. 3. Finally, conclusions are drawn in Sec. 4.

2 An outline of theory used

In this section, we have presented briefly the formal aspects of projected shell model (PSM). For more details, one can refer to the review article on PSM [27, 28]. PSM calculations are of the shell model type, but, unlike shell model, it uses the deformed Nilsson potential. The Nilsson parameters κ and μ, used in the Nilsson potential for the construction of deformed basis, are taken from Ref. [29]. Three major shells (N= 3, 4 and 5) for both neutrons and protons are taken for the formation of configuration space. The inclusion of deformed basis has the advantage of incorporating important nuclear pairing correlations more readily. Further, with the inclusion of deformed basis, rotational symmetry is violated which is restored by the standard angular momentum projection technique [30]. Besides, the pairing correlations are added by performing BCS calculations.

In this work, we have used the following Hamiltonian:

$$\hat{H} = \hat{H}_0 - \frac{1}{2}\chi \sum_{\mu} \hat{Q}_{\mu} Q^{\dagger}_{\mu} - G_M \hat{P}^{\dagger}\hat{P} - G_Q \sum_{\mu} \hat{P}^{\dagger}_{\mu}\hat{P}_{\mu} \tag{1}$$

where $\hat{H}_0$ is the spherical single-particle shell model Hamiltonian which contains proper spin–orbit coupling whose strengths (i.e. Nilsson parameters κ and μ) are taken in such a manner that they reproduce the best fit of available experimental data [21–23, 31–33]. The second term in the Hamiltonian denotes the quadrupole–quadrupole two-body interaction and χ represents its strength. The value of χ is adjusted by the self-consistent relation in such a way that the input quadrupole deformation ϵ_2 and the one resulting from the HFB procedure agrees with each other. The third and fourth terms represent monopole–pairing and quadrupole–pairing forces, respectively. The pairing strengths generally influence the level spacing within a band, and in the present calculations, their values are adjusted in such a way that known energy gap can be generated. The parameter G_M represents the monopole–pairing strength and is defined as

$$G_M = \left[G_1 \mp G_2 \frac{N-Z}{A}\right] A^{-1}(\text{MeV}) \tag{2}$$

with "−" for neutrons and "+" for protons. The choice of these strengths depends on the size of the single-particle space in the calculations. In the present calculations, for both positive and negative parity, the values of G_1 and G_2 are taken as 21.20 and 12.70, respectively. The quadrupole–pairing strength G_{Q} is assumed to be proportional to G_{M}, with the proportionality constant being fixed as 0.16 for positive parity and 0.18 for negative parity in the present calculations. The parameters of the basis deformation ϵ_2 and ϵ_4 used in our calculations for each nucleus are given in Table 1. Different configurations (one and three quasi-particle states) are built within the chosen basis.

3 Results and discussion

In the present calculations, the valance space is truncated by the inclusion of the states within an energy window of 3.5 MeV, both for protons and for neutrons, around the Fermi surface. This determines the size of the basis space. In the next step, these basis states are

Table 1 Deformation parameters used as input in the present calculations of $^{145-149}$Pm nuclei

Nucleus	Positive parity		Negative parity	
	ε_2	ε_4	ε_2	ε_4
^{145}Pm	0.175	0.028	0.180	0.018
^{147}Pm	0.175	0.020	0.180	0.018
^{149}Pm	0.160	0.025	0.160	0.018

projected to good angular momentum states and the projected basis is then used to diagonalize the shell model Hamiltonian which, in turn, gives rise to the yrast energy spectra. Further, the resulting wave functions are subsequently used to calculate various nuclear structure properties including reduced transition probabilities. These results along with some other nuclear structure properties obtained through PSM calculations and their comparison with the experimentally available data are presented in the following subsections.

3.1 Back-bending in moment of inertia

The phenomenon of back-bending in moment of inertia is an important feature of rotational spectra of deformed nuclei. Since yrast band is formed by states of both 1-*qp* (which generally forms the lower spin states) and 3-*qp* bands (which form the major components of the higher spins), the phenomenon of back-bending carries important information on the interplay and alignment between the 1-*qp* band and multi-*qp* bands. In Fig. 1, we have made comparison of the PSM results with experimental data for positive as well as negative parities states for odd-mass$^{145-149}$Pm isotopes. We plot twice the kinetic moment of inertia $2\Im^{(1)}$ as a function of square of rotational frequency ($\hbar^2\,\omega^2$). These quantities are defined as [34].

$$2\Im^{(1)} = \frac{(2I-1)}{\omega}, \tag{3}$$

$$\omega = \frac{E_\gamma}{\sqrt{(I+1)(I+2)-K^2}-\sqrt{(I-1)I-K^2}} \tag{4}$$

where $E_\gamma = E(I) - E(I-2)$.

3.1.1 Positive parity

For ^{145}Pm (Fig. 1a), the experimental and theoretical back-bending occur at the spin value of $15/2^+$ and $11/2^+$ corresponding to almost the same values of rotational frequencies of 0.1611 $\hbar^2\,\omega^2$ and 0.1756 $\hbar^2\,\omega^2$, respectively. On the other hand, for ^{147}Pm (Fig. 1b), the experimental back-bending in moment of inertia is reproduced exactly at the same value of spin $15/2^+$ by PSM results and this spin value also corresponds to almost the same rotational frequencies of 0.1052 $\hbar^2\,\omega^2$and 0.1044 $\hbar^2\,\omega^2$, respectively. By examining the moment of inertia pattern for ^{149}Pm in Fig. 1c, back-bending is observed to occur experimentally at the spin $I = 15/2^+$corresponding to the rotational frequency of 0.0885 $\hbar^2\,\omega^2$, whereas PSM calculations predict the occurrence of back-bending corresponding to rotational frequency of 0.1470 $\hbar^2\,\omega^2$ at the spin $I = 19/2^+$.

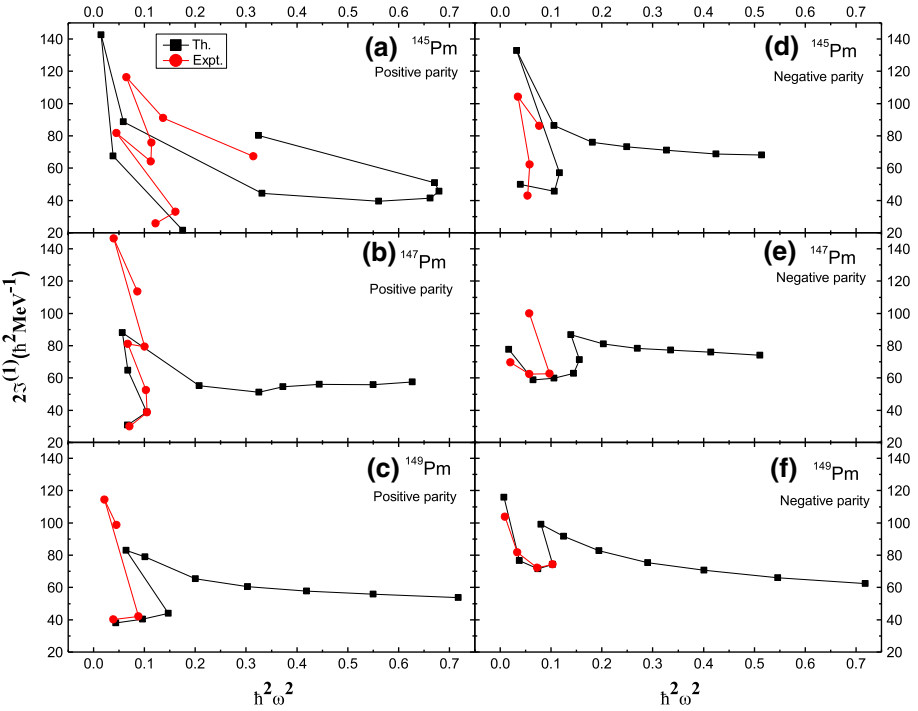

Fig. 1 PSM results for twice the kinetic moment of inertia $[2\Im^{(1)}(\hbar^2 MeV^{-1})]$ plotted against the angular frequency squared $(\hbar^2\omega^2)$ for positive parity **a** ^{145}Pm, **b** ^{147}Pm and **c** ^{149}Pm and negative parity **d** ^{145}Pm, **e** ^{147}Pm and **f** ^{149}Pm. The experimental data [21–23, 31–33] are also shown for comparison

3.1.2 Negative parity

From Fig. 1d, it is found that, for negative parity ^{145}Pm, the experimental back-bending is observed at the spin value of $19/2^-$ corresponding to rotational frequency of 0.0578 $\hbar^2\ \omega^2$, whereas the PSM calculations predict the back-bending at spin $21/2^-$ corresponding to rotational frequency of 0.1059 $\hbar^2\ \omega^2$, respectively. For ^{147}Pm, in Fig. 1e, experimentally observed back-bending is found to occur at the spin $23/2^-$ corresponding to the rotational frequency of 0.0971 $\hbar^2\ \omega^2$ whereas PSM calculations also predict a back-bending but a little delayed at the spin $31/2^-$ corresponding to rotational frequency 0.1558 $\hbar^2\ \omega^2$. Further, for ^{149}Pm (Fig. 1 f), the PSM calculations predict the back-bending at the spin $27/2^-$ at rotational frequency 0.1033 $\hbar^2\ \omega^2$, while, due to less experimental data available in this nucleus, no experimental back-bending could be found to occur in this nucleus.

It is quite noteworthy from Fig. 1 that the comparison between theory and experiment is overall satisfactory. The observed variation in $\Im^{(1)}$ in odd-mass $^{145-149}$Pm isotopes is an important indication for structural changes in wave functions as it is well known that nucleons in high-j orbits respond sensitively to the rotation and can easily align their spin direction along with the system rotation, and this observation is successfully reproduced by PSM calculations. This change in the moment of inertia $\left(\Im^{(1)}\right)$ with rotational frequency may arise due to the interaction between various 1-qp and 3-qp bands which will be discussed thoroughly in the next subsection. Furthermore, the positive parity experimental data show several back-bending phenomena in $^{145-147}$Pm, whereas the theoretical results are not enough

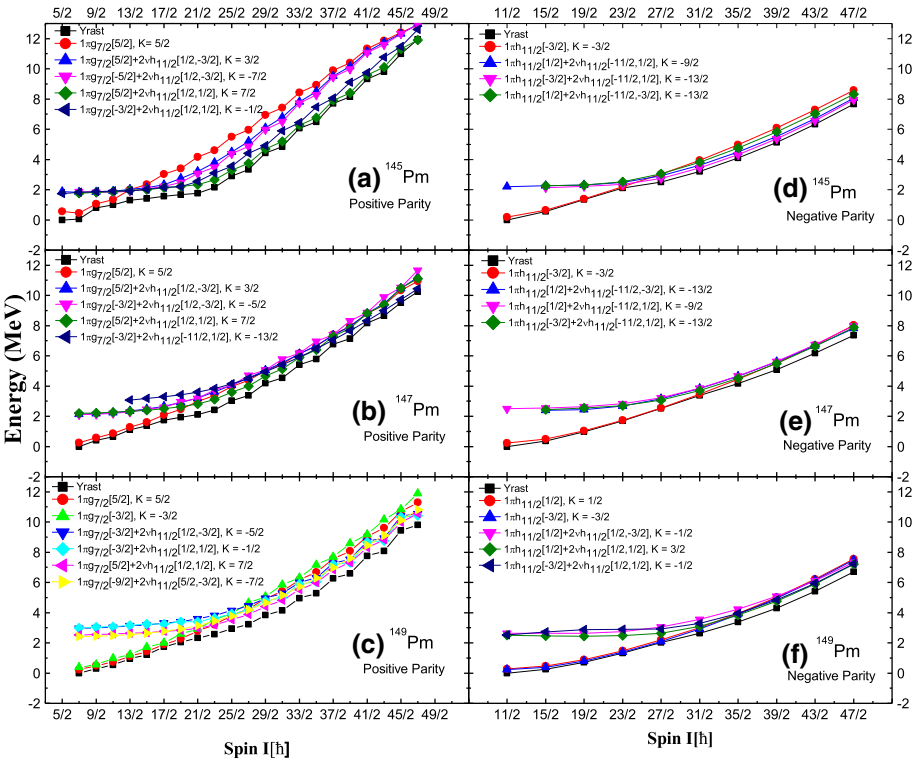

Fig. 2 Band diagrams for positive parity **a** ^{145}Pm, **b** ^{147}Pm and **c** ^{149}Pm and negative parity **d** ^{145}Pm, **e** ^{147}Pm and **f** ^{149}Pm

to reproduce these phenomena, as shown in Fig. 1. This could be because of the reason that the valence space of the present calculations is not enough to describe the high-spin states from $33/2^+$.

3.2 Analysis of band diagrams

The results of back-bending phenomenon in odd-mass $^{145-149}$Pm isotopes indicate the presence of rotational alignment of quasiparticles in particular orbitals of these nuclei. For odd-mass nuclei, it is associated with crossings between bands with 1-*qp* and 3-*qp* configurations. In the present work, 1-*qp* configurations arise from the deformed proton $g_{7/2}$ orbit for positive parity and $h_{11/2}$ orbit for negative parity, while 3-*qp* ones consist of these proton 1-*qp* configurations plus a pair of $h_{11/2}$ neutrons. Thus, the plot of energies of various angular-momentum-projected multi-quasi-particle bands as a function of spin, generally known as band diagrams, helps us to understand the back-bending effects which are found to be present (discussed above as per Fig. 1) in the odd-mass $^{145-149}$Pm isotopes.

In Fig. 2, band energies of each angular-momentum-projected configuration are plotted as functions of spin for both positive and negative parity bands. The energy of a band κ is defined by

$$E_\kappa(I) = \frac{\left\langle \phi_\kappa \middle| \hat{H}\hat{P}^I_{KK} \middle| \phi_\kappa \right\rangle}{\left\langle \phi_\kappa \middle| \hat{P}^I_{KK} \middle| \phi_\kappa \right\rangle} \tag{5}$$

Here, $\hat{P}^I_{KK}$ is the angular momentum projection operator.

3.2.1 Positive parity

For ^{145}Pm, it is clear from Fig. 2a that at low spins yrast states up to spin $11/2^+$ are formed by 1-*qp* band $1\pi g_{7/2}$ [5/2], $K = 5/2$. However, as spin increases from $11/2^+$ to $13/2^+$, this 1-*qp* band is approached by several 3-*qp* bands and band crossing occurs at spin $13/2^+$. These 3-*qp* bands are identified as $1\pi g_{7/2}$ [5/2] + $2\nu h_{11/2}$ [1/2, − 3/2], $K = 3/2$, $1\pi g_{7/2}$ [− 5/2] + $2\nu h_{11/2}$ [− 1/2, − 3/2], $K = -7/2$, $1\pi g_{7/2}$ [5/2] + $2\nu h_{11/2}$ [1/2, 1/2], $K = 7/2$ and $1\pi g_{7/2}$ [− 3/2] + $2\nu h_{11/2}$ [1/2, 1/2], $K = -1/2$. These superimposed 3-*qp* bands continue to form yrast spectra up to spin $17/2^+$. After that, i.e. from spin $19/2^+$ onwards, the 3-*qp* band $1\pi g_{7/2}$ [5/2] + $2\nu h_{11/2}$ [1/2, 1/2], $K = 7/2$ remains lowest in energy and leads to the formation of yrast states.

It can be seen from Fig. 2b that the yrast states for ^{147}Pm up to spin $19/2^+$ are found to build on the 1-*qp* band $1\pi g_{7/2}$ [5/2], $K = 5/2$. At the next spin, i.e. $21/2^+$, a strong interaction between the 1-*qp* band and a 3-*qp* band is seen which results in band crossing. This interacting 3-*qp* band forms the yrast spectra up to the spin $31/2^+$ and is identified as $1\pi g_{7/2}$ [5/2] + $2\nu h_{11/2}$ [1/2, 1/2], $K = 7/2$. Afterwards, another 3-*qp* band identified as $1\pi g_{7/2}$ [− 3/2] + $2\nu h_{11/2}$ [− 11/2, 1/2], $K = -13/2$ appears as main contributor towards the formation of yrast spectra for the rest of the spin values. Moreover, two more 3-*qp* bands having configurations $1\pi g_{7/2}$ [− 3/2] + $2\nu h_{11/2}$ [1/2, − 3/2], $K = -5/2$ and $1\pi g_{7/2}$ [5/2] + $2\nu h_{11/2}$ [1/2, − 3/2], $K = 3/2$ are also found lower in energy and shown in Fig. 2b.

Talking about ^{149}Pm (Fig. 2c), for the spin range $I = 7/2^+$ to $21/2^+$, the yrast band has the main component of the two 1-*qp* bands $1\pi g_{7/2}$ [5/2], $K = 5/2$ and $1\pi g_{7/2}$ [− 3/2], $K = -3/2$. This configuration is strongly disturbed by a 3-*qp* band $1\pi g_{7/2}$ [5/2] + $2\nu h_{11/2}$[1/2, 1/2], $K = 7/2$, and the band crossing occurs at spin $23/2^+$. As the spin increases beyond $23/2^+$, few more 3-*qp's* with configurations $1\pi g_{7/2}$ [− 3/2] + $2\nu h_{11/2}$ [1/2, − 3/2], $K = -5/2$, $1\pi g_{7/2}$ [− 3/2] + $2\nu h_{11/2}$ [1/2, 1/2], $K = -1/2$ and $1\pi g_{7/2}$ [− 9/2] + $2\nu h_{11/2}$ [5/2, − 3/2], $K = -7/2$ bands dive down in energy and contribute towards the formation of yrast spectra up to the last calculated spin.

3.2.2 Negative parity

It is clear from the band diagram for ^{145}Pm, shown in Fig. 2d, that up to the spin $23/2^-$, the yrast band is composed of 1-*qp* band, $1\pi h_{11/2}$[− 3/2], $K = -3/2$, which is then crossed by a 3-*qp* bands with configuration: $1\pi h_{11/2}$[− 11/2] + $2\upsilon h_{11/2}$[− 3/2, 1/2], $K = -13/2$. Thus, band crossing occurs at spin $23/2^-$. This 3-*qp* band along with two more 3-*qp* bands: $1\pi h_{11/2}$[1/2] + $2\upsilon h_{11/2}$[− 11/2, 1/2], $K = -9/2$ and $1\pi h_{11/2}$[1/2] + $2\upsilon h_{11/2}$[− 11/2, − 3/2], $K = -13/2$, are found to be lower in energy contributing to the yrast energy levels up to the last calculated spin.

In the case of ^{147}Pm (Fig. 2e), the yrast band up to a spin of $33/2^-$ is built by1-*qp* $1\pi h_{11/2}$[− 3/2], $K = -3/2$. As we reach the spin $35/2^-$, various 3-*qp* bands approach the above-mentioned 1-*qp* band and the interaction becomes maximum at $35/2^-$, where band crossing occurs, and the 3-*qp* band $1\pi h_{11/2}$[− 3/2] + $2\upsilon h_{11/2}$[− 11/2, 1/2], $K = -13/2$

crosses the 1-*qp* band and forms the rest of the yrast spectra along with two more 3-*qp* bands: $1\pi h_{11/2}[1/2] + 2\upsilon h_{11/2}[-11/2, -3/2]$, $K = -13/2$ and $1\pi h_{11/2}[1/2] + 2\upsilon h_{11/2}[-11/2, 1/2]$, $K = -9/2$.

Finally, for ^{149}Pm (see Fig. 2f), up to the spin of $31/2^-$, the yrast spectra arise because of superimposition of two 1-*qp* bands, $1\pi h_{11/2}[1/2]$, $K = 1/2$ and $1\pi h_{11/2}[-3/2]$, $K = -3/2$. At spin $31/2^-$, band crossing occurs and a 3-*qp* band having configuration $1\pi h_{11/2}[1/2] + 2\upsilon h_{11/2}[1/2, 1/2]$, $K = 3/2$ becomes lower in energy and contributes towards the formation of yrast along with two more 3-*qp* bands having configurations $1\pi h_{11/2}[1/2] + 2\upsilon h_{11/2}[1/2, -3/2]$, $K = -1/2$ and $1\pi h_{11/2}[-3/2] + 2\upsilon h_{11/2}[1/2, 1/2]$, $K = -1/2$ up to the last calculated spin.

Further, from the above discussion on band diagrams, we can say that the observed backbending in ^{145,147,149}Pm isotopes may be described as being happening due to the crossing of the ground band, i.e. 1-*qp* band consisting of single proton ($\mathbf{1\pi g_{7/2}}$ for positive parity and $1\pi h_{11/2}$ for negative parity) with another 3-*qp* rotational band consisting of one proton and two neutrons ($1\pi g_{7/2} + 2\upsilon h_{11/2}$ for positive parity and $1\pi\ h_{11/2} + 2\upsilon h_{11/2}$ for negative parity) having a larger moment of inertia.

3.3 Yrast spectra

In the present work, PSM calculations have been carried out by assuming an axial symmetry in the deformed basis where each band (1-*qp* or 3-*qp*) can be assigned with a K quantum number. We have already discussed the various 1-*qp* and 3-*qp* bands and the interaction between them which leads towards the formation of yrast spectra both for the positive and for the negative parity. The yrast spectra are obtained by diagonalization of the Hamiltonian in the deformed basis constructed using Nilsson potential, which, in turn, corresponds to the configuration mixing or band mixing in shell model. Calculated yrast energy levels for both positive and negative parity of odd-mass $^{145-149}$Pm isotopes are plotted against the spin in Figs. 3 and 4, respectively. Further, to check the degree of accuracy, a comparison of these calculated results is made with the experimentally available data [23–25, 33–35] in the same figures. These comparisons show the efficacy of the applied PSM technique as the experimental data are very well reproduced.

Theoretically, we have been able to obtain the data on positive and negative parity yrast states in these nuclei up to a maximum spin of 47/2, whereas experimental data on the yrast states for the positive parity are available up to a maximum spin value $39/2^+$, $41/2^+$ and $23/2^+$ for ^{145}Pm, ^{147}Pm and ^{149}Pm, respectively, and $27/2^-$ for negative parity of all the three isotopes ^{145}Pm, ^{147}Pm and ^{149}Pm. Experimentally, the band heads for positive parity states of ^{145}Pm, ^{147}Pm and ^{149}Pm have been observed as $5/2^+$, $7/2^+$ and $7/2^+$, respectively, whereas for negative parity states, the band head spin of all these $^{145-149}$Pm has been measured as $11/2^-$. In our calculations, we are successful to reproduce the band heads for both positive and negative parities yrast bands of odd-mass $^{145-149}$Pm isotopes. Moreover, by analysing the band diagrams, we can say that the proposed band structures in the present work are built on 1-*qp* bands at low spins, whereas at higher spins, the yrast states are built on 3-*qp* bands.

3.4 Analysis of the wave functions

For better evaluation of nuclear structure, one requires a detailed analysis of the wave functions. In the present PSM calculations, the eigenvalues of energy along with the amplitude of wave functions have been obtained by diagonalization of the total Hamiltonian. In Fig. 5, we have presented the average of the amplitudes of the wave functions corresponding to various

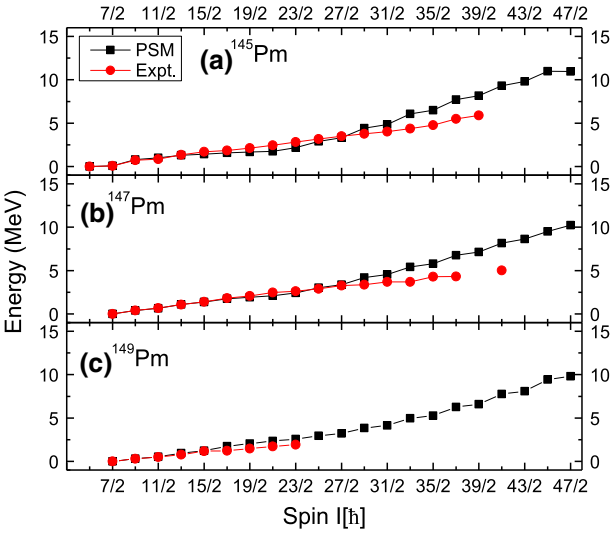

Fig. 3 Comparison of calculated and experimentally available yrast spectra for positive parity **a** ^{145}Pm, **b** ^{147}Pm and **c** ^{149}Pm. The experimental data [21–23, 31–33] are also shown for comparison

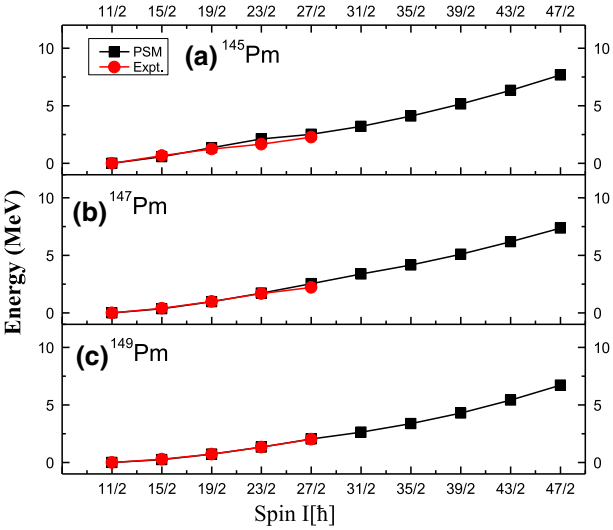

Fig. 4 Comparison of calculated and experimentally available yrast spectra for negative parity **a** ^{145}Pm, **b** ^{147}Pm and **c** ^{149}Pm. The experimental data [21–23, 31–33] are also shown for comparison

1-*qp* and 3-*qp* bands responsible for the formation of positive as well as negative parity yrast spectra of odd-mass $^{145-149}$Pm isotopes. The interactions between wave functions of 1-*qp* bands and 3-*qp* bands, shown in these plots, clearly depict the origin of certain characteristics phenomena in these nuclei, like back-bending in moment of inertia, band crossing, configuration mixing, etc. (explained earlier in the previous subsections). It should be noted that average amplitudes of the wave functions corresponding to 1-*qp* bands cross the average amplitude of wave functions corresponding to 3-*qp* bands at the same values of spins

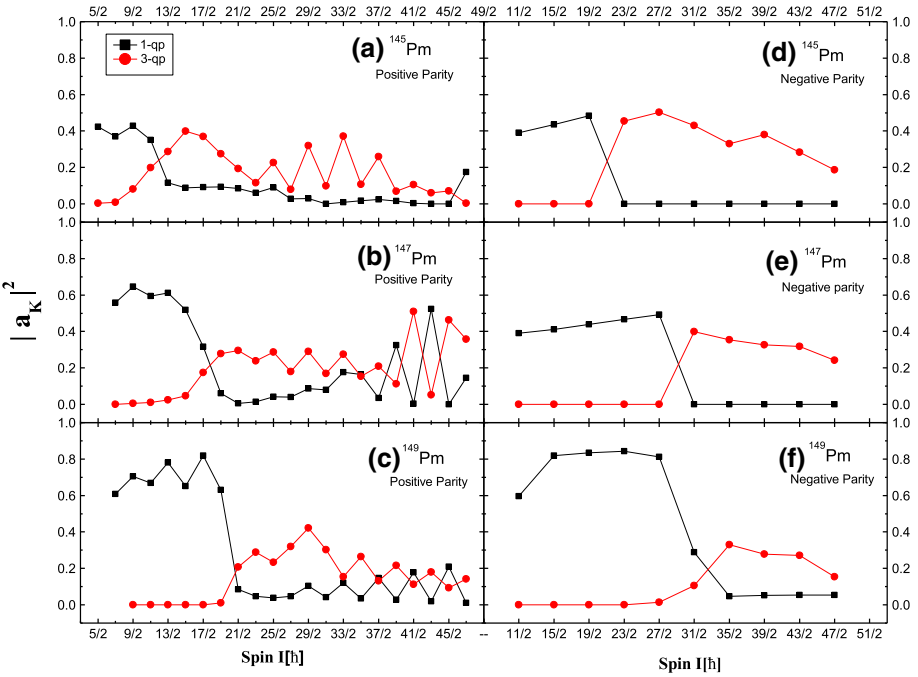

Fig. 5 Probability amplitude of various projected K-configurations in the wave functions of the positive parity yrast bands for **a** ^{145}Pm, **b** ^{147}Pm and **c** ^{149}Pm and the negative parity yrast bands for **d** ^{145}Pm, **e** ^{147}Pm and **f** ^{149}Pm

at which band crossing takes place. Further, the trends of probability amplitudes show that yrast bands for $^{145-149}$Pm isotopes have well-defined structures built on 1-*qp* configurations at lower spins, but at higher spins, the yrast states are dominated by 3-*qp* bands. Further, it is quite clear that the experimental negative parity yrast states are quite well reproduced for the entire spin range by the present PSM calculations, but, for positive parity states, there is a little variation in the data in the high-spin regime. Thus, the present calculated PSM wave functions are well enough to reproduce and explain the various observed nuclear structure phenomena at lower spins in odd-mass $^{145-149}$Pm nuclei. With this motivation, we have used the wave functions obtained through PSM calculations to calculate the reduced transition probabilities which are discussed in the next section.

3.5 Reduced transition probabilities

The reduced electric quadrupole transition probability $B(E2)$ (from an initial state ($I_i = I$) to a final state ($I_f = I - 2$)) is defined by

$$B(E2, I \rightarrow I-2) = \frac{e^2}{2I+1}\left|\Psi^{I-2}\right|\left|\hat{Q}_2\right|\left|\Psi^{I}\right|^2 \tag{6}$$

where the operator $\hat{Q}_2$ is related to the quadrupole operators.

In the present calculations, we have taken the standard values of effective charges, i.e. 1.5e for protons and 0.5e for neutrons. The effective charges are fixed for all nuclei studied in this work without any individual adjustment. Generally, these values measure the extent

Table 2 B($E2$) values for positive parity ^{145,147,149}Pm isotopes

Transition	^{145}Pm	^{147}Pm	^{149}Pm
$9/2^+ \rightarrow 5/2^+$	0.12313	–	–
$11/2^+ \rightarrow 7/2^+$	0.08146	0.10357	0.05794
$13/2^+ \rightarrow 9/2^+$	0.17527	0.16179	0.19853
$15/2^+ \rightarrow 11/2^+$	0.12823	0.20038	0.16508
$17/2^+ \rightarrow 13/2^+$	0.19084	0.24067	0.2492
$19/2^+ \rightarrow 15/2^+$	0.16365	0.24801	0.22592
$21/2^+ \rightarrow 17/2^+$	0.19679	0.28417	0.27354
$23/2^+ \rightarrow 19/2^+$	0.18599	0.27484	0.25979
$25/2^+ \rightarrow 21/2^+$	0.20094	0.3111	0.28941
$27/2^+ \rightarrow 23/2^+$	0.20033	0.29247	0.27957
$29/2^+ \rightarrow 25/2^+$	0.2044	0.32962	0.30162
$31/2^+ \rightarrow 27/2^+$	0.20086	0.30569	0.29164
$33/2^+ \rightarrow 29/2^+$	0.19745	0.34337	0.31091
$35/2^+ \rightarrow 31/2^+$	0.20853	0.31703	0.29971

Table 3 B($E2$) values for negative parity ^{145,147,149}Pm isotopes

Transition	^{145}Pm	^{147}Pm	^{149}Pm
$15/2^- \rightarrow 11/2^-$	0.18805	0.2092	0.16508
$19/2^- \rightarrow 15/2^-$	0.23098	0.25803	0.22592
$23/2^- \rightarrow 19/2^-$	0.25503	0.28416	0.25979
$27/2^- \rightarrow 23/2^-$	0.2715	0.30029	0.27957
$31/2^- \rightarrow 27/2^-$	0.28433	0.31161	0.29164
$35/2^- \rightarrow 31/2^-$	0.28698	0.3206	0.29971

up to which quadrupole distortions are present in the structure of a nucleus. The PSM results on the reduced electric transition probabilities ($B(E2)$) for positive as well as negative parity yrast band in $^{145-149}$Pm isotopes are given in Tables 2 and 3, respectively. It should be noted that experimental data on $B(E2)$ values for positive as well as negative parity yrast states on these nuclei are not available, so these results could serve as motivation for experimentalists.

Further, using PSM wave function, one can also calculate reduced magnetic transition probability $B(M1)$. The reduced magnetic dipole transition probability $B(M1)$ from initial state ($I_i = I$) to final state ($I_f = I - 1$) is given by

$$B(M1, I \rightarrow I-1) = \frac{e^2}{2I+1} \left| \Psi^{I-1} \right| \left| \hat{M}_l \right| \left| \Psi^{I} \right|^2 \tag{7}$$

where the magnetic dipole operator is defined as

$$\hat{\mathrm{M}}_1^{\tau} = g_l^{\tau} \hat{j}^{\tau} + \left(g_s^{\tau} - g_l^{\tau} \right) \hat{s}^{\tau}.$$

Here, τ is either π or ν, and g_l and g_s are the orbital and the spin gyromagnetic factors, respectively. In the present work, we use the free values for g_l, whereas for g_s, the free values were damped by a factor of 0.85. The standard free values of g_l and g_s for protons and neutrons are

$$g_l^{\pi} = 1,\ g_l^{\nu} = 0,\ g_s^{\pi} = 5.586 \times 0.85,\ g_s^{\nu} = -3.826 \times 0.85.$$

Table 4 B(M1) values for positive parity ^{145,147,149}Pm isotopes

Transition	^{145}Pm	^{147}Pm	^{149}Pm
$7/2^+ \rightarrow 5/2^+$	0.08579	–	–
$9/2^+ \rightarrow 7/2^+$	0.15432	0.02819	0.03652
$11/2^+ \rightarrow 9/2^+$	0.01257	0.05353	0.04163
$13/2^+ \rightarrow 11/2^+$	0.03759	0.03842	0.06579
$15/2^+ \rightarrow 13/2^+$	0.00907	0.07176	0.05093
$17/2^+ \rightarrow 15/2^+$	0.01899	0.03882	0.08087
$19/2^+ \rightarrow 17/2^+$	0.00913	0.08101	0.06407
$21/2^+ \rightarrow 19/2^+$	0.02189	0.03876	0.0905
$23/2^+ \rightarrow 21/2^+$	0.0073	0.0849	0.08044
$25/2^+ \rightarrow 23/2^+$	0.03498	0.03954	0.09581
$27/2^+ \rightarrow 25/2^+$	0.00531	0.08601	0.0948
$29/2^+ \rightarrow 27/2^+$	0.04232	0.04143	0.09747
$31/2^+ \rightarrow 29/2^+$	0.00221	0.08557	0.10267
$33/2^+ \rightarrow 31/2^+$	0.02541	0.04495	0.09713
$35/2^+ \rightarrow 33/2^+$	0.07216	0.07784	0.10088

The calculated values of magnetic transition probabilities $B(M1)$ for positive parity yrast band of the nuclei under study are given in Table 4. The usual staggering pattern of $B(M1)$ values can be seen from these data. Again, no experimental data on $B(M1)$ values are available for yrast bands on these nuclei.

In order to check the accuracy of the calculated $B(E2)$ and $B(M1)$ values, we decided to compare the theoretically calculated electromagnetic transition strength ratio ($B(M1)/B(E2)$ with the values of transition strength ratios which are extracted from the experimentally measured intensities [33, 34] using the relation given in Ref. [35]. Figure 6 shows the comparison of experimental and calculated values of $B(M1)/B(E2)$ ratio for the positive parity yrast band of odd-mass $^{145-149}$Pm isotopes. The theoretical values of $B(M1)/B(E2)$ ratio appear to agree with the measured values which authenticate the efficacy of the PSM technique and validate the calculated $B(\mathbf{E}2)$ and $B(M1)$ values for the yrast band of the nuclei under study. Moreover, no experimental data are available on $B(M1)$ and $B(E2)$ for the yrast states, so the calculated values of these parameters in the present work will prove useful for various theoretical as well as experimental research groups.

4 Summary and perspectives

PSM calculations, in the present work, have been able to reproduce quite successfully the positive as well as negative parity yrast states in odd-mass Pm nuclei with neutron number $82 < N < 90$. The intrinsic structure of positive and negative parity yrast states has been found to be built on $\pi g_{7/2} \otimes \nu h_{11/2}$ and $\pi h_{11/2} \otimes \nu h_{11/2}$configuration, respectively. The reduced transition probabilities, i.e. $B(M1)$ and $B(E2)$, have also been calculated for these nuclei. However, experimental data on $B(M1)$ and B($E2$) values for these nuclei are not available, yet we are able to confirm their accuracy by comparing their ratio ($B(M1)/B(E2)$) with the corresponding values obtained from experimentally measured intensities. Moreover, the calculated values of reduced transition probabilities, in the present work, would strengthen

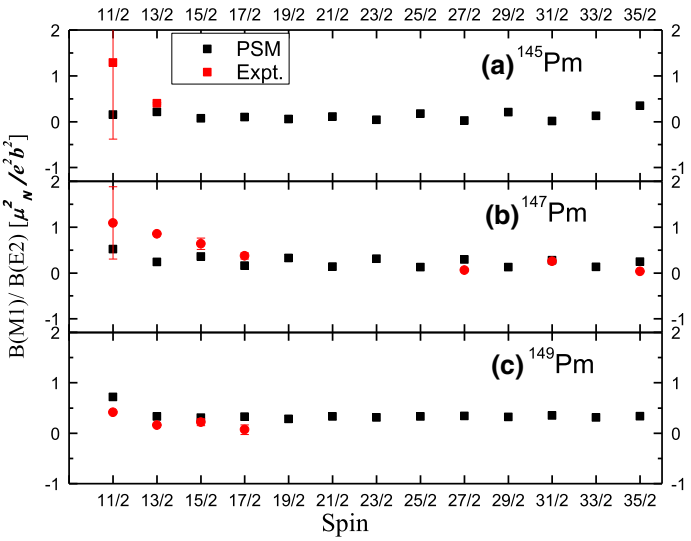

Fig. 6 Comparison of calculated $B(M1)/B(E2)$ transition strengths ratios with the experimental values obtained from the measured intensity of transitions for positive parity bands in **a** ^{145}Pm, **b** ^{147}Pm and **c** ^{149}Pm. The experimental data are taken from Refs. [31–33]

the understanding of the intricate structure of these nuclei at high spins and will serve as a motivation for the experimentalists to work for extraction of these values. The origin of back-bending phenomenon in $^{145-149}$Pm isotopes is very well explained through band diagrams as well as by PSM wave functions

Acknowledgements One of the authors, Suram Singh, acknowledges the financial support from University Grants Commission (UGC), MHRD, Govt. of India, under UGC BSR Start-up grant no. F.30-412/2018(BSR).

References

1. R.F. Casten, D.D. Warner, D.S. Brenner, R.L. Gill, Phys. Rev. Lett. **47**, 1433 (1981)
2. A. Ercan, R. Broda, P. Kleinheiz, M. Piiparinen, R. Julin, J. Blomqvist, Z. Phys. **329**, 63 (1988)
3. M. Piiparinen, Y. Nagai, P. Kleinheiz, M.C. Bosca, B. Rubio, M. Lach, J. Blomqvist, Z. Phys. A **338**, 417 (1991)
4. A. Kuhnert, D. Alber, H. Grawe, H. Kluge, K.H. Maier, W. Reviol, X. Sun, E.M. Beck, A.P. Byrne, H. Hiibel, J.C. Bacelar, M.A. Deleplanque, R.M. Diamond, F.S. Stephens, Phys. Rev. C **46**, 484 (1992)
5. E. Kleinheinz, Nuov. Cim. A **81**, 140 (1984)
6. W.R. Phillips, I. Ahmad, H. Emling, R. Holzman, R.V.F. Janssens, T.-L. Khoo, M.W. Drigert, Phys. Rev. Lett. **57**, 3257 (1986)
7. W.J. Vermeer, M.K. Khan, A.S. Mowbray, J.B. Fitzgerald, J.A. Cizewski, B.J. Varley, J.L. Durell, W.R. Phillips, Phys. Rev. C **42**, RI183 (1990)
8. W. Urban et al., Phys. Lett. B **258**, 293 (1991)
9. C.J. Pearson, W.R. Phillips, J.L. Durell, B.J. Varley, W.J. Vermeer, W. Urban, M.K. Khan, Phys. Rev. C **49**, 10239 (1994)
10. T. Glasmacher, D.D. Caussyn, P.D. Cottle, T.D. Johnson, K.W. Kemper, P.C. Womble, Phys. Rev. C **45**, 1619 (1992)
11. M. Lach et al., Z. Phys. A **341**, 25 (1991)
12. W.R. Daniels, D.C. Hoffman, Phys. Rev. C **4**, 919 (1971)
13. M. Shibata et al., Appl. Radiat. Isot. **44**, 923 (1993)
14. A. Taniguchi et al., J. Phys. Soc. Jpn. **65**, 3824 (1996)

15. T. Karlewski et al., Z. Phys. A **322**, 177 (1985)
16. R.C. Greenwood, R.A. Anderl, J.D. Cole, H. Willmes, Phys. Rev. C **35**, 1965 (1987)
17. M. Shibata et al., Eur. Phys. J. A **31**, 171 (2007)
18. D.G. Burke, G. Lovhoiden, E.R. Flynn, J.W. Sunier, Phys. Rev. C **18**, 693 (1978)
19. I.S. Lee et al., Nucl. Phys. A **371**, 111 (1981)
20. J.K. Hwang, A.V. Ramayya, J.H. Hamilton, S.H. Liu, K. Li, H.L. Crowell, C. Goodin, Y.X. Luo, J.O. Rasmussen, S.J. Zhu, Phys. Rev. C **80**, 037304 (2009)
21. Ch. Vieu et al., Phys. Rev. C **54**, 2264 (1996)
22. W. Urban et al., Nucl. Phys. A **587**, 541 (1995)
23. M.A. Jones et al., Nucl. Phys. A **609**, 201 (1996)
24. D. Sharma, A. Gupta, S. Singh, A. Bharti, Chin. J. Phys. **54**, 42 (2016)
25. V. Rani, P. Verma, S. Singh, M. Rajput, A. Bharti, G.H. Bhat, J.A. Sheikh, Chin. Phys. C **44**, 094107 (2020)
26. M. Ogawa, R. Broda, K. Zell, P.J. Daly, P. Kleinheinz, Phys. Rev. Lett. **41**, 289 (1978)
27. K. Hara, Y. Sun, Int. J. Mod. Phys. E **4**, 637 (1995)
28. Y. Sun, Phys. Scr. **91**, 043005 (2016)
29. S.G. Nilsson et al., Nucl. Phys. A **131**, 1 (1969)
30. P. Ring, P. Schuck, *The Nuclear Many-Body Problem* (Springer, New York, 1980)
31. E. Browne, J.K. Tuli, Nucl. Data Sheets **110**, 507 (2009)
32. N. Nica, Citation: Nucl. Data Sheets **110**, 749 (2009)
33. Balraj Singh, Nucl. Data Sheets **102**, 1 (2004)
34. A. Ibáñnez-Sandoval, M.E. Ortiz, V. Velázquez, A. Galindo-Uribarri, P.O. Hess, Y. Sun, Phys. Rev. C **83**, 034308 (2011)
35. M. Sugawara et al., Nucl. Phys. A **699**, 450 (2002)